Journal of
Materials Chemistry C

ROYAL SOCIETY
OF CHEMISTRY

PAPER

View Article Online
View Journal

Check for updates

Cite this: DOI: 10.1039/d6tc01000h

Bias-dependent layer-resolved Raman evidence for interfacial asymmetry in vertical graphene/MoSe$_2$/graphene junctions on SiO$_2$/Si substrates

Youngro Lee[a,b] and Jaewu Choi*[a]

Received 27th March 2026,
Accepted 2nd June 2026

DOI: 10.1039/d6tc01000h

rsc.li/materials-c

Vertical graphene/MoSe$_2$/graphene (Gr/MoSe$_2$/Gr) junctions are promising for tunable electronics as well as optoelectronics based on vertical transport. To identify the junction properties of a vertically stacked Gr/MoSe$_2$/Gr junction on SiO$_2$/Si, we combine *in situ* bias-dependent Raman spectroscopy with temperature-dependent transport measurements. At zero bias, the Raman response of the two graphene electrodes appears as a single overlapped feature. Under finite bias, this response separates into two distinct contributions, which allows layer-resolved extraction of the chemical potential shifts of the two graphene electrodes. The extracted shifts are strongly asymmetric, with Gr$_{bot}$ showing a consistently smaller response than Gr$_{top}$ under both bias polarities. This result indicates that the junction is better described as an asymmetric back-to-back Schottky diode with a less electrostatically tunable bottom interface. The device also exhibits a clear hysteresis loop in the cyclic current–voltage characteristics, indicating history-dependent hysteretic transport characteristics. At room temperature, the transport remains nearly symmetric, but the polarity asymmetry becomes stronger at higher temperature. A plausible origin is an asymmetric junction formed by different defect environments at the two interfaces. MoSe$_2$ can contain intrinsic Se vacancies. Upon additional exposure of the upper MoSe$_2$ surface, some of these vacancy sites can undergo O substitution, whereas the lower interface can retain a stronger Se vacancy character. These in-gap Se vacancy states may contribute to Fermi level pinning. A temperature-dependent change in this pinning condition may further change the effective barrier profile and thereby enhance the transport asymmetry. These results show that interface quality and transfer history play a central role in determining the electrostatic response of vertical Gr/MoSe$_2$/Gr heterostructures.

Introduction

Electrically tunable stacked van der Waals heterostructure devices based on the atomically thin two-dimensional layers are promising for electronics, optoelectronics, sensing, memory, and quantum applications.[1–9] Among them, vertically stacked graphene/transition-metal-dichalcogenide/graphene (Gr/TMD/Gr) heterostructures offer a unique platform for the aforementioned applications.[10–14] An atomically thin TMD spacer provides an atomically defined barrier as well as electrical and optical functionality, while graphene electrodes enable efficient electrostatic tunability because the density of states near the Dirac point is low.[15–17] However, bias-driven interactions in Gr/TMD/Gr junctions are often inferred indirectly. Many studies rely on static spectroscopy or on current–voltage (*I*–*V*) characteristics alone, which does not uniquely determine how charge redistributes between the upper and lower graphene layers under an applied bias.[18–20] In practice, the measured vertical transport can mix contributions from tunneling through the spacer, parasitic leakage paths, and contact-related effects, obscuring the connection between device characteristics and layer-specific electrostatics.

Among common TMD spacers, MoSe$_2$ is particularly convenient because it provides a semiconducting barrier with strong optical transitions in the visible and a clear Raman fingerprint that can be used as an internal structural reference.[21–23] In the monolayer limit, MoSe$_2$ exhibits a direct optical gap near 1.55 eV, which highlights its suitability for optoelectronic operation, while thicker layers evolve toward a smaller indirect gap.[24,25] In addition, the interlayer spacing in bulk MoSe$_2$ is about 0.65 nm,[26,27] providing a simple geometric scale for few layer thickness estimates in stacked junctions. These considerations raise the question of whether the two Gr/MoSe$_2$ interfaces in a real vertically stacked device remain electrostatically equivalent after ambient transfer and stacking.

---

[a] *Quantum Information Display Laboratory, Department of Information Display, Kyung Hee University, 26, Kyungheedae-ro, Dongdaemun-gu, Seoul, 02447, Republic of Korea. E-mail: jaewuchoi@khu.ac.kr*

[b] *Laboratory for Quantum Magnetism, Institute of Physics, École Polytechnique Fédérale de Lausanne (EPFL), CH-1015 Lausanne, Switzerland*

In this context, bilayer $MoSe_2$ devices provide a useful platform for examining whether the two Gr/$MoSe_2$ interfaces remain electrostatically equivalent under applied bias, particularly when interfacial residues, trapped charges, and local inhomogeneity perturb the electrostatic landscape. In this work, we investigate a vertically stacked bilayer Gr/$MoSe_2$/Gr junction on SiO_2/Si by combining *in situ* bias-dependent Raman spectroscopy and temperature-dependent DC transport. This approach allows us to compare the bias response of the two graphene electrodes within the same device and to examine how interfacial asymmetry emerges in the electrical and spectroscopic response.

Experimental details

Graphene was synthesized on a 35 μm thick Cu foil by chemical vapor deposition (CVD).[28–31] Prior to growth, the Cu foil was annealed at 1000 °C for 30 min under Ar (100 sccm) and H_2 (50 sccm). Graphene growth was then carried out at 1000 °C using CH_4 (5 sccm) for 8 min. For transfer, Poly(methyl methacrylate) (PMMA) (40 g L^{-1} in 1,2-dichlorobenzene) was spin coated onto the graphene at 2000 rpm to form a PMMA-supported film. The underlying Cu was etched in a 0.7 M $FeCl_3$ solution. After Cu etching, the PMMA/Gr film was rinsed sequentially through fresh deionized water baths several times to remove residual $FeCl_3$ and ionic contaminants before being transferred onto the target substrate.

The graphene film was cut into rectangular pieces of approximately 10 mm × 2.5 mm and transferred diagonally onto a 10 mm × 10 mm SiO_2/Si substrate with a 300 nm SiO_2 layer. After transfer, the sample was baked at 150 °C for 15 min, immersed in acetone at 60 °C for 1 h to remove PMMA, and annealed at 350 °C in an Ar and H_2 atmosphere for 2 h.

A commercial $MoSe_2$ film (Sixcarbon Technology, 10 mm × 10 mm on SiO_2/Si substrate) was cut into approximately 5 mm × 5 mm pieces and transferred onto the bottom graphene using a PMMA-assisted wet transfer. The $MoSe_2$ piece was aligned approximately with the edges of the substrate, without intentional rotation, followed by the same PMMA removal and annealing procedure. A second graphene strip of approximately 10 mm × 2.5 mm was then transferred onto the $MoSe_2$ layer using the same method. The two graphene strips were arranged in a crossed geometry so that their overlap occurred only through the $MoSe_2$ region, yielding a nominal junction area of approximately A = 2.5 mm × 2.5 mm. The effective transport area may be smaller in the presence of local interfacial inhomogeneity. Electrical contacts to the top and bottom graphene electrodes were made using silver paste, which was allowed to dry in ambient conditions prior to measurements.

The Raman spectra of the device were measured using a T64000 JobinYvon system with a 532 nm laser and an optical power of 0.6 mW. The scattered signal was collected in a backscattering geometry using a 100× objective, giving a spot diameter of approximately 1 μm. *In situ* bias-dependent Raman measurements were performed at $V = -5$, 0, and +5 V applied between the two graphene electrodes, where a positive bias corresponds to applying $+V$ to the bottom graphene electrode with respect to the top graphene electrode.

I-V characteristics were measured using a Keithley 6430 femtoammeter under ambient conditions. In the single pass mode, the bias was swept from −5 to +5 V in 0.25 V steps. For cyclic measurements, the bias was swept in the sequence 0 to +5 to 0 to −5 to 0 V with the same 0.25 V step size. Throughout this work, forward bias ($V > 0$) denotes the positive bias voltage applied to the bottom graphene electrode, whereas reverse bias ($V < 0$) denotes the negative bias voltage applied to the top graphene electrode. Temperature-dependent measurements were performed using the same setup with the device mounted on a hot plate at 328 and 423 K. For each temperature, the device was held until the current response stabilized before the voltage sweep.

Results and discussion

Device overview and baseline characterization

Fig. 1 summarizes the device geometry and baseline Raman fingerprints of the Gr/$MoSe_2$/Gr heterostructure on Si/SiO_2. Fig. 1(a) shows the device layout, Raman probe positions, and an enlarged schematic of the bilayer $MoSe_2$ region between the top and bottom graphene electrodes. The enlarged schematic includes representative defect-related sites as a structural guide for the later discussion of interfacial asymmetry. Fig. 1(b) shows the optical microscope image of the fabricated device, while Fig. 1(c) presents a representative Raman spectrum measured in the full stack region. The spectrum contains the $MoSe_2$ vibrational mode together with the graphene G and 2D bands and the Si substrate features. No additional Raman features attributable to PMMA residue were resolved within the measured spectral range. The inset provides an expanded view of the $MoSe_2$ mode region. The out-of-plane A_{1g} mode appears at about 241.3 cm^{-1}, consistent with bilayer $MoSe_2$.[35–38]

Fig. 1(d) compares the graphene G and 2D bands measured in the three regions as marked in Fig. 1(a). The G and 2D bands were fitted separately using Lorentzian functions, and the extracted peak positions and FWHM values are summarized in Table 1. Relative to the Gr only region (1), both peaks shift to lower wavenumbers in the $MoSe_2$-containing regions (2,3), whereas the FWHM remains comparable across all three regions. These systematic shifts indicate that the graphene Raman response is modified by the local interfacial environment in the Gr/$MoSe_2$/Gr heterostructure. At V = 0 V, the graphene Raman response is consistent with hole doping, with the Fermi level located about 0.22 eV below the Dirac point.[39]

To further support the bilayer assignment inferred from the $MoSe_2$ A_{1g} position in Fig. 1(c), we also consider a simple optical attenuation estimate based on the fitted graphene Raman intensities in Fig. 1(d). For $MoSe_2$ at λ = 532 nm, we take $k \approx 1.55$, corresponding to an absorption coefficient $\alpha = 4\pi k/\lambda \approx 4.1 \times 10^7\ m^{-1}$.[40,41] In the first approximation, the measured Raman intensity from the Gr_{bot} scales as $\exp(-2\alpha d)$ due to attenuation of both the incident and scattered light through a

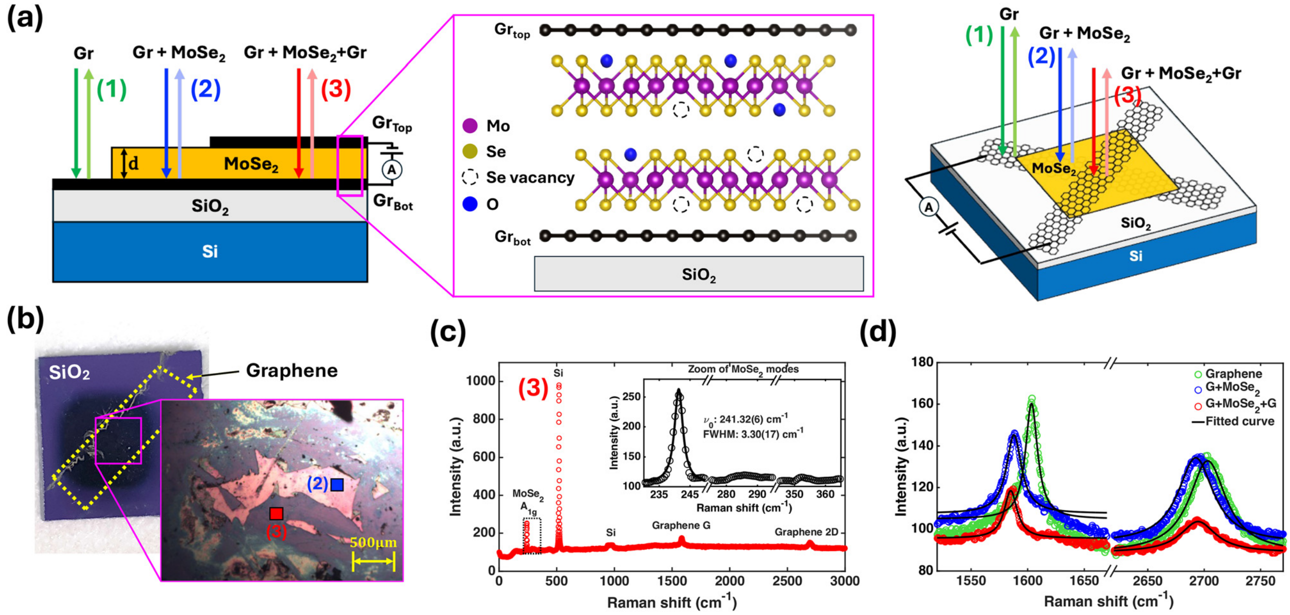

Fig. 1 (a) Schematics of the vertical Gr/MoSe$_2$/Gr heterostructure fabricated on a Si/SiO$_2$ substrate. Raman measurements were performed in three representative regions: (1) Gr only (green), (2) Gr/MoSe$_2$ (blue), and (3) the full Gr/MoSe$_2$/Gr stack (red). The enlarged schematic on the right illustrates the bilayer MoSe$_2$ region between the top and bottom graphene electrodes, with representative Se vacancies and O-related sites included to visualize the possible interfacial asymmetry.[32,33] This atomic structural image of MoSe$_2$ and graphene was drawn with the program VESTA.[34] (b) Optical microscope image of the fabricated device on the Si/SiO$_2$ substrate. The yellow dashed outline indicates the transferred strip. The pink box marks the region enlarged in the inset, which shows the junction area in more detail. The red and blue squares indicate the laser probe positions corresponding to the regions defined in panel (a). (c) Representative Raman spectrum measured in region (3), corresponding to the Gr/MoSe$_2$/Gr stack. The labeled peaks identify the corresponding spectral features. The inset highlights the MoSe$_2$ mode region. (d) Enlarged Raman spectra around the graphene G and 2D bands measured in regions (1)–(3). Solid black lines are independent Lorentzian fits to the graphene G and 2D peaks.

Table 1 Lorentzian fit results for the graphene G and 2D bands measured in the three regions defined in Fig. 1. Values in parentheses denote the standard deviation in the final reported digits. Uncertainty in I_{2D}/I_G was estimated by standard error propagation from the fitted amplitude and width parameters

Parameters	Gr only	Gr/MoSe$_2$	Gr/MoSe$_2$/Gr
G position (cm^{-1})	1603.40(5)	1587.90(5)	1585.00(3)
G FWHM (cm^{-1})	13.01(30)	16.24(17)	13.89(18)
2D position (cm^{-1})	2703.10(5)	2695.20(5)	2694.60(10)
2D FWHM (cm^{-1})	39.75(30)	38.30(24)	38.13(38)
I_{2D}/I_G	0.77(5)	1.09(4)	0.65(3)

MoSe$_2$ layer of thickness d. Using the ratio of the fitted graphene G peak maxima between region (2) and region (1), ($I_{Gr+MoSe_2}/I_{Gr} \approx 0.90$), we obtain $d \approx 1.3$ nm. This value is consistent with the thickness of bilayer MoSe$_2$ ($\approx 2 \times 0.65$ nm).[26,27] Because graphene Raman intensities can also be affected by charge transfer, optical interference on Si/SiO$_2$, and strain, we treat this attenuation-based estimate only as a qualitative consistency check rather than an independent thickness determination.

Bias-dependent interactions between graphene layers

Fig. 2 combines bias-dependent transport and Raman analyses of the vertical Gr/MoSe$_2$/Gr junction. Panels (a)–(c) provide an effective electrical parameterization of the measured I–V response, while panels (d)–(f) track the layer-resolved evolution of the graphene Raman features under applied bias.

The measured I–V characteristics in Fig. 2(a) suggest that the present device is better viewed as a back-to-back Schottky junction. For a simplified analysis, we nevertheless apply the Cheung method within a single-diode thermionic-emission picture.[43] The resulting parameters should therefore be regarded as effective quantities rather than unique microscopic junction properties. Fig. 2(b) shows that $dV/d\ln I$ varies in slope across the measured current range, indicating that no single parameter set describes the full response. We therefore divide the data into four current intervals, labeled (i) to (iv), and perform separate linear fits in each region.

The corresponding Cheung function in Fig. 2(c) provides a complementary effective description of the barrier-related response. In the low-current intervals, the apparent series resistance remains fairly consistent between the two analyses, with representative values of about 38 W. The corresponding effective barrier-related energies are on the order of 0.3–0.4 eV, whereas the apparent ideality factor is modest only in the low-current intervals and becomes nonphysical at higher current. Taken together, these results further indicate that no single parameter set describes the full I–V response. We therefore use the Cheung analysis only as an effective parameterization of the measured junction behavior. The full region-dependent fitting results are provided in the SI.

To probe the electrostatic state of each graphene electrode more directly, we therefore turn to bias-dependent Raman spectroscopy. Fig. 2(d) shows *in situ* Raman spectra of the graphene G and 2D bands measured at $V = +5$, 0, and -5 V.

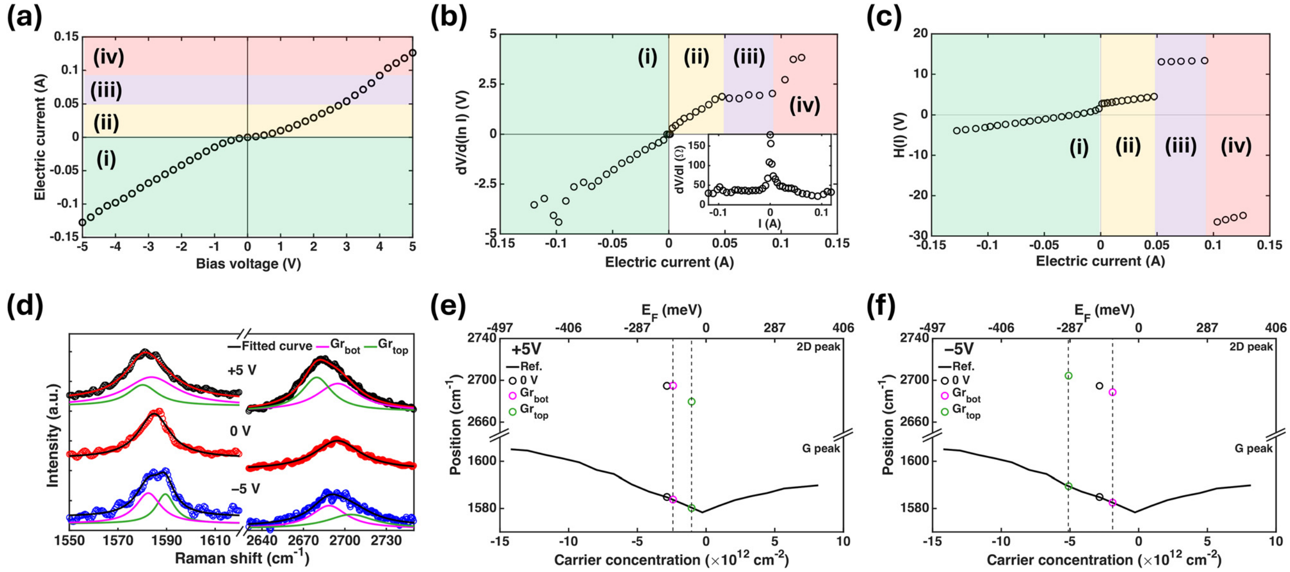

Fig. 2 (a) I–V characteristics of the Gr/MoSe$_2$/Gr device. The current windows labeled (i) to (iv), defined from the interval-dependent analysis in panel (b), are indicated for reference. (b) Cheung plot dV/d(ln I) *versus* I, constructed from the data in panel (a). The four current windows (i) to (iv) were fitted separately because the slope changes across the measured range. The inset shows the differential resistance dV/dI derived from the same I–V curve. (c) Cheung function $H(I)$ *versus* I, where $H(I) \equiv V - nk_BT/q \times \ln(I/AA^*T^2)$, evaluated using the interval-dependent n values extracted from panel (b). Here A = 6.25 mm^2 is the nominal geometric overlap area of the junction, and A^* = 2.4 × 10^{-5} A mm^{-2} K^{-2} is the Richardson constant.[42] The same current windows are indicated. (d) *In situ* Raman spectra of the graphene G and 2D band recorded at applied biases of +5, 0, and −5 V. Open symbols denote the data, and the total fits are shown by black and red curves. The fitted graphene components are shown by the pink and green curves, assigned to the Gr$_{bot}$ and Gr$_{top}$ electrodes, respectively. (e) Peak positions of the G and 2D bands extracted from the fits at +5 V for Gr$_{bot}$ (pink) and Gr$_{top}$ (green), shown together with the corresponding 0 V values. The extracted G peak positions are converted to carrier concentration and Fermi energy using the reference calibration (solid black curve).[39] Error bars are smaller than the marker size and are therefore not visible. (f) Same analysis as in panel (e) for −5 V, shown together with the 0 V values for comparison.

At 0 V, the G band is well described by a single Lorentzian, indicating that the two graphene layers have similar Fermi levels within the present spectral resolution. Under finite bias, however, the G band broadens markedly and deviates from a single-peak profile, even though the applied bias is the only experimental parameter changed. The 2D bands show a similar broadening and line shape evolution under finite bias. Although strain and spatial inhomogeneity can also affect Raman line shapes, the correlated response of the G and 2D bands is more naturally explained by electrostatic doping.[44–46]

The fitted Raman peak positions were converted to carrier concentration using the Raman doping calibration shown by the black solid line in Fig. 2(e) and (f).[39] The carrier concentration n_{2D} was converted to the Fermi energy through

$$E_F = \hbar v_F \sqrt{\pi |n_{2D}|}. \tag{1}$$

The extracted fit parameters and derived electronic quantities are summarized in Table 2. Fig. 2(e) and (f) summarize the extracted values at V = +5 and −5 V, respectively, together with the corresponding 0 V position for comparison. The doping sign was assigned as p-type based on Hall measurements reported previously for graphene grown under comparable conditions on SiO$_2$/Si.[30,31] At V = +5 V, Gr$_{bot}$ and Gr$_{top}$ shift toward the Dirac point by about ΔE_F = 17(8) meV and 84(9) meV, respectively. At V = −5 V, Gr$_{bot}$ shifts toward the Dirac point by about ΔE_F = 39(8) meV, whereas Gr$_{top}$ shifts away from it by about 74(6) meV.

These results show that the two graphene electrodes do not respond electrostatically in an equivalent manner under applied bias. In both bias polarities, Gr$_{bot}$ exhibits a consistently smaller chemical potential shift than Gr$_{top}$. The finite bias Raman response therefore reveals a clear interface-dependent asymmetry in the electrostatic response of the junction.

Table 2 Peak positions and FWHM values extracted from Lorentzian fits to the bias-dependent Raman spectra in Fig. 2. The carrier concentration n_{2D} was estimated from the fitted G peak positions using the Raman doping calibration in ref. 39, and the corresponding Fermi energy E_F was obtained from the graphene Dirac relation. The values in parentheses denote the standard deviation in the final reported digits. Uncertainties in n_{2D} and E_F were estimated by propagating the fitted G peak uncertainty

Condition	G position (cm^{-1})	G FWHM (cm^{-1})	2D position (cm^{-1})	2D FWHM (cm^{-1})	n_{2D} (×10^{12} cm^{-2})	E_F (meV)
+5 V, Gr$_{bot}$	1583.8(5)	25.8(20)	2694.9(4)	37.5(9)	−2.40(14)	−199(6)
+5 V, Gr$_{top}$	1580.2(6)	15.1(7)	2679.6(2)	26.5(4)	−1.05(13)	−132(8)
0 V, both Gr	1584.9(1)	15.7(4)	2694.7(2)	40.3(9)	−2.84(12)	−216(5)
−5 V, Gr$_{bot}$	1582.5(3)	12.5(5)	2688.6(10)	31.3(27)	−1.89(12)	−177(6)
−5 V, Gr$_{top}$	1589.5(3)	9.2(9)	2704.4(14)	41.3(32)	−5.09(12)	−290(3)

This reduced bias response of Gr_{bot} is consistent with lower electrostatic tunability at the $MoSe_2/Gr_{bot}$ interface. One possible microscopic origin is a nonequivalent defect environment at the two interfaces. In particular, additional air exposure of the upper $MoSe_2$ surface prior to the Gr_{top} transfer may modify the local defect population relative to the lower interface.

Hysteretic transport associated with interfacial trapping

Fig. 3 shows a clear hysteresis loop in the cyclic *I*–*V* response, indicating that the transport depends on the sweep history. Repeated cyclic measurements under the same bias protocol showed reproducible hysteretic behavior. This behavior is consistent with a history-dependent interfacial process, such as charge trapping and detrapping, at the $MoSe_2/Gr_{bot}$ interface.[32,33] Combined with the reduced bias response of Gr_{bot} observed in the Raman analysis, the cyclic transport curves suggest that the $MoSe_2/Gr_{bot}$ side is less electrostatically tunable due to interfacial charge trapping. The defect-related states near the $MoSe_2/Gr_{bot}$ partially screen the applied bias and pin the graphene Fermi level. Furthermore, the slow charging and discharging of these states during the voltage sweep can modify the local barrier profile, producing the observed hysteretic transport which can be viewed as a potential defect-driven memory device. The hysteretic transport therefore aligns with the same interfacial asymmetry identified spectroscopically, further indicating that the bottom interface is the less ideally tunable side of the junction.

Temperature-dependent enhancement of transport asymmetry

The temperature-dependent transport in Fig. 4 further highlights the interfacial asymmetry identified by Raman spectroscopy. Under positive bias, the current increases with temperature, whereas under negative bias the current magnitude decreases. This contrasting temperature response leads to a marked increase in the rectifying ratio and shows that the polarity asymmetry becomes stronger at elevated temperature. The temperature dependence therefore does not merely enhance conduction, but selectively amplifies the pre-existing polarity asymmetry of the junction.

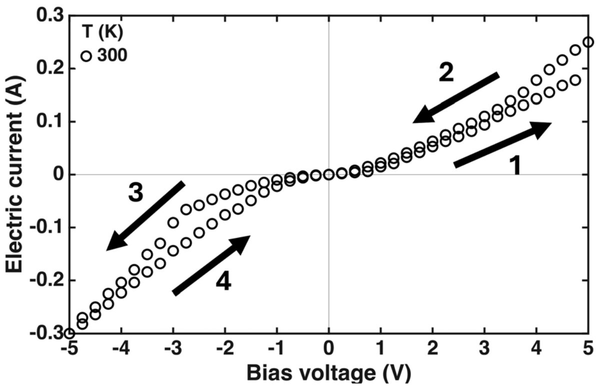

Fig. 3 Hysteretic transport in the vertical $Gr/MoSe_2/Gr$ junction. Cyclic *I*–*V* characteristic measured at 300 K, showing a clear hysteresis loop. The numbers 1 to 4 indicate the measurement sequence and corresponding scan direction within the hysteresis loop.

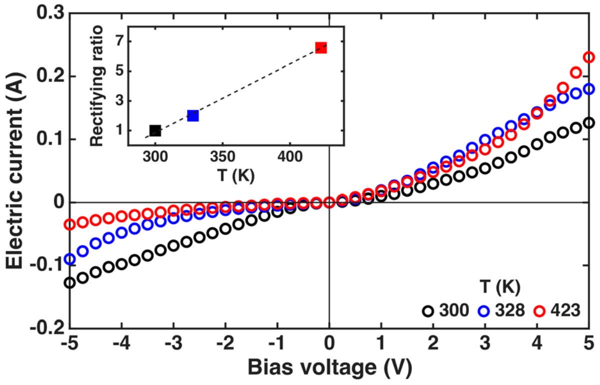

Fig. 4 Temperature-dependent enhancement of transport asymmetry in the vertical $Gr/MoSe_2/Gr$ junction. Temperature-dependent *I*–*V* characteristics measured in a separate single-pass sweep from −5 to + 5 V at 300, 328, and 423 K. With increasing temperature, the response becomes more asymmetric, with enhanced current under positive bias and suppressed current under negative bias. The inset shows the rectifying ratio, defined as |*I*(+5 V)/*I*(−5 V)|, as a function of temperature.

The enhancement of the rectification shown in the inset of Fig. 4 is the central feature showing the temperature-dependent interfacial behaviors. If the temperature dependence were governed only by thermionic activation process, the current increase in both polarities would be expected unlike what we observed in Fig. 4. In contrast, the present device shows opposite temperature trends in the bias directions. The positive-bias branch becomes more conductive, whereas the negative-bias branch becomes more blocking. Such opposite temperature trends are difficult to explain solely by a global series-resistance increase or irreversible contact degradation, since these effects would generally be expected to suppress the current magnitude in both bias polarities. This behavior suggests that the effective $MoSe_2/Gr$ barrier profile changes with temperature in a polarity-dependent manner.

Consistent with this behavior, a possible explanation is that temperature-dependent charge redistribution at the bottom interface changes the initial pinning condition and is associated with a change in the effective barrier profile under negative bias. In this picture, the additional blocking contribution under negative bias can outweigh the usual thermal enhancement of carrier injection, leading to a reduced current magnitude and an increased rectifying ratio at elevated temperature.

Modeling of interfacial asymmetry

Building on the results above, we use the qualitative schematic band diagrams in Fig. 5 to provide a unified picture of the present junction in terms of interface-specific asymmetry. In vertically assembled Gr/TMD/Gr junctions, the two interfaces are not necessarily equivalent in practice, even when the nominal stack is symmetric. Processing history and oxygen exposure can introduce nonequivalent local environments at the top and bottom interfaces, which in turn may lead to different electrostatic responses under applied bias. Fig. 5(a) shows an idealized zero bias alignment without interfacial defects, based on the bilayer $MoSe_2$ band gap and representative energy offsets reported for

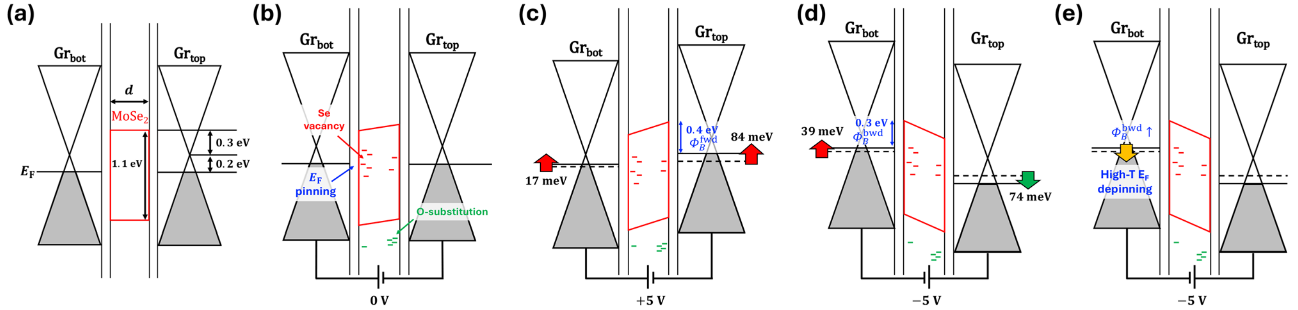

Fig. 5 Qualitative schematic band diagrams of the vertical Gr/MoSe$_2$/Gr junction used to guide the discussion. (a) Reference zero-bias band alignment of the Gr/MoSe$_2$/Gr stack, showing the MoSe$_2$ band gap and representative energy offsets used in the discussion.[25,32,33,47] (b) Modified zero-bias alignment including defect-related states, illustrating the interfacial asymmetry and partial pinning inferred from experiment.[25,47,48] The red gradient is introduced schematically to represent a defect-rich interfacial region and the resulting asymmetry and partial pinning inferred from the Raman and transport data.[32,33,49] (c) Schematic band diagram at $V = +5$ V including the layer-resolved graphene chemical-potential shifts extracted from the Raman analysis. (d) Schematic band diagram at $V = -5$ V at 300 K including the Raman-derived chemical-potential shifts. (e) Proposed band diagram at $V = -5$ V at elevated temperature, illustrating a temperature-dependent change in the Gr$_{bot}$ pinning condition and the resulting increase in the effective Schottky barrier at the Gr$_{bot}$/MoSe$_2$ interface. The effective MoSe$_2$/Gr interfacial barriers are indicated schematically to emphasize that the vertical transport is governed by the bias-dependent barrier profile.

graphene contacted MoSe$_2$.[25,47] Fig. 5(b) presents a more realistic zero bias reference for the present device by introducing defect-related states near the MoSe$_2$/Gr$_{bot}$ interface. In this schematic picture, Se-vacancy-induced in-gap states and O-substitution-related states below the valence band edge can give rise to Fermi level pinning.[32,33] Fig. 5(c) and (d) then schematically illustrate how the band profile evolves under positive and negative bias when the experimentally extracted graphene chemical potential shifts are taken into account. Fig. 5(e) further extends this picture to high temperature under negative bias, where the band profile is modified to reflect the enhanced effective Schottky barrier inferred from the temperature-dependent transport.

Taken together, the bias-dependent Raman shifts, the hysteretic transport response, and the temperature-dependent polarity asymmetry indicate that the Gr/MoSe$_2$/Gr junction cannot be described as a fully symmetric vertical stack, but is better understood as an asymmetric back-to-back Schottky junction. A possible origin of this asymmetry lies in the different defect environments that can develop at the two MoSe$_2$ interfaces during device assembly. The atomic schematic in Fig. 1(a) provides a structural basis for this picture by illustrating representative Se vacancies and O-related sites in the bilayer MoSe$_2$ region between the two graphene electrodes. In MoSe$_2$, Se vacancies are commonly formed and generally act as n-type donor-like defects, whereas exposure of the upper MoSe$_2$ surface to ambient conditions prior to graphene transfer can promote partial passivation or substitution by oxygen. Such O-related states are expected to lie below the MoSe$_2$ valence band edge. Therefore, even a defect-containing junction can become electrostatically asymmetric when the top and bottom interfaces are exposed to different local chemical environments. Within this picture, the Gr$_{bot}$/MoSe$_2$ side can retain a larger Se vacancy contribution and therefore exhibit stronger Fermi level pinning, so that the corresponding graphene chemical potential does not shift as strongly under applied bias. This interpretation is consistent with the Raman analysis, which reveals a reduced bias induced chemical potential response for the interface associated with the negative bias limiting branch. At elevated temperature, a partial weakening of this pinning can increase the effective Schottky barrier on the negative bias side, and if this increase outweighs the usual thermally assisted carrier emission, the current magnitude can decrease rather than increase. In this way, the temperature-dependent transport can be understood as a polarity-dependent evolution of the effective barrier response within an already asymmetric back-to-back Schottky junction, consistent with a temperature-dependent change in the pinning condition at elevated temperature. Within this qualitative picture, interface engineering emerges as a practical route for controlling hysteretic transport and temperature-dependent barrier modulation in vertical 2D junctions. In particular, encapsulation and surface passivation may help tune defect asymmetry and thereby modify the resulting transport response.

Conclusions

In conclusion, we identify bias-dependent interfacial asymmetry, history-dependent hysteretic transport characteristics, and temperature-dependent changes in the effective barrier profile in a vertically stacked bilayer Gr/MoSe$_2$/Gr junction by combining *in situ* bias-dependent Raman spectroscopy and temperature-dependent transport characterizations. Under finite bias, the graphene Raman response evolves from a single-component line shape into two distinct contributions, enabling layer-resolved extraction of the chemical-potential shifts of the two graphene electrodes. The extracted shifts are strongly asymmetric, with Gr$_{bot}$ showing a consistently smaller response than Gr$_{top}$, indicating that the bottom interface is less electrostatically tunable.

The hysteretic I–V response and the polarity-dependent temperature response are both consistent with Fermi level pinning at the MoSe$_2$/Gr$_{bot}$ interface. This behavior may reflect a nonequivalent defect environment created during transfer and stacking. In particular, Se-related defects may remain more prominent at one interface. At the other interface, additional air exposure of the upper $MoSe_2$ surface before the transfer of Gr_{top} may promote O-related defect modification, thereby producing an asymmetric junction. At higher temperature, a temperature-dependent change in the pinning condition at the bottom interface may increase the effective barrier height under negative bias and further enhance the transport asymmetry.

More broadly, these results show that the electrostatic response of vertical Gr/$MoSe_2$/Gr is governed not only by the nominal layer sequence but also by the interfacial condition established during transfer and stacking. This highlights that interface engineering, either to suppress defect-related pinning and recover larger electrostatic chemical-potential shifts or to control pinning in a controlled manner, could provide a useful route to tuning the operation of future electronic and optoelectronic devices.

Author contributions

Youngro Lee: conceptualization, investigation, methodology, formal analysis, data curation, visualization, writing – original draft, writing – review and editing. Jaewu Choi: conceptualization, supervision, project administration, resources, funding acquisition, writing – review and editing.

Conflicts of interest

There are no conflicts to declare.

Data availability

The data supporting this article are available.

The supplementary information (SI) provides a more detailed analysis of the data presented in Fig. 2(b) and (c), using the same dataset as that used in the main text. See DOI: https://doi.org/10.1039/d6tc01000h.

Acknowledgements

This research was supported by Basic Science Research Program through the National Research Foundation of Korea (NRF) funded by the Ministry of Education (NRF-2019R1F1A1063643, RS-2026-25491298 and BK21 FOUR Program).

Notes and references

1 W. Liao, Y. Huang, H. Wang and H. Zhang, *Appl. Mater. Today.*, 2019, **16**, 435–455.
2 H. L. Hou, C. Anichini, P. Samorí, A. Criado and M. Prato, *Adv. Funct. Mater.*, 2022, **32**, 2207065.
3 P. V. Pham, S. C. Bodepudi, K. Shehzad, Y. Liu, Y. Xu, B. Yu and X. Duan, *Chem. Rev.*, 2022, **122**, 6514–6613.
4 H. Xu, Y. Xue, Z. Liu, Q. Tang, T. Wang, X. Gao, Y. Qi, Y. P. Chen, C. Ma and Y. Jiang, *Small Sci.*, 2024, **4**, 2300213.
5 H. Huang, S. Shi, J. Zha, Y. Xia, H. Wang, P. Yang, L. Zheng, S. Xu, W. Wang, Y. Ren, Y. Wang, Y. Chen, H. P. Chan, J. C. Ho, Y. Chai, Z. Wang and C. Tan, *Nat. Commun.*, 2025, **16**, 3836.
6 C. Y. Wang, S. J. Liang, S. Wang, P. Wang, L. Zhu'an, Z. Wang, A. Gao, C. Pan, C. Liu, J. Liu, H. Yang, X. Liu, W. Song, C. Wang, B. Cheng, X. Wang, K. Chen, Z. Wang, K. Watanabe, T. Taniguchi, J. J. Yang and F. Miao, *Sci. Adv.*, 2020, **6**, eaba6173.
7 X. Ma, L. Wang, G. Huang, S. Gong, Y. Qi, J. Zhang, R. Zhao, Y. Li, G. Liu, C. Ma, J. Gao and Y. Jiang, *Appl. Phys. Lett.*, 2022, **120**, 061107.
8 H. Henck, D. Mauro, D. Domaretskiy, M. Philippi, S. Memaran, W. Zheng, Z. Lu, D. Shcherbakov, C. N. Lau, D. Smirnov, L. Balicas, K. Watanabe, T. Taniguchi, V. I. Fal'ko, I. Gutiérrez-Lezama, N. Ubrig and A. F. Morpurgo, *Nat. Commun.*, 2022, **13**, 3917.
9 D. Shen, H. B. Yang, T. Patel, D. A. Rhodes, T. Timusk, Y. N. Zhou, N. Y. Kim and A. W. Tsen, *ACS Nano*, 2024, **18**, 11193–11199.
10 L. Britnell, R. V. Gorbachev, R. Jalil, B. D. Belle, F. Schedin, A. Mishchenko, T. Georgiou, M. I. Katsnelson, L. Eaves, S. V. Morozov, N. M. Peres, J. Leist, A. K. Geim, K. S. Novoselov and L. A. Ponomarenko, *Science*, 2012, **335**, 947–950.
11 A. K. Geim and I. V. Grigorieva, *Nature*, 2013, **499**, 419–425.
12 W. J. Yu, Y. Liu, H. Zhou, A. Yin, Z. Li, Y. Huang and X. Duan, *Nat. Nanotechnol.*, 2013, **8**, 952–958.
13 K. Zhang, X. Fang, Y. Wang, Y. Wan, Q. Song, W. Zhai, Y. Li, G. Ran, Y. Ye and L. Dai, *ACS Appl. Mater. Interfaces*, 2017, **9**, 5392–5398.
14 S. Chanarsa, N. Semakul, J. Jakmunee, P. Iamprasertkun, P. H. Aubert and K. Ounnunkad, *J. Energy Storage*, 2024, **98**, 113083.
15 T. Georgiou, R. Jalil, B. D. Belle, L. Britnell, R. V. Gorbachev, S. V. Morozov, Y. J. Kim, A. Gholinia, S. J. Haigh, O. Makarovsky, L. Eaves, L. A. Ponomarenko, A. K. Geim, K. S. Novoselov and A. Mishchenko, *Nat. Nanotechnol.*, 2012, **8**, 100–103.
16 Y. Liu, N. O. Weiss, X. Duan, H. C. Cheng, Y. Huang and X. Duan, *Nat. Rev. Mater.*, 2016, **1**, 16042.
17 A. D. Squires, L. Z. Song, S. Kuriakose, J. Du and T. van der Laan, *npj 2D Mater. Appl.*, 2025, **9**, 77.
18 H. Tian, Z. Tan, C. Wu, X. Wang, M. A. Mohammad, D. Xie, Y. Yang, J. Wang, L. J. Li, J. Xu and T. L. Ren, *Sci. Rep.*, 2014, **4**, 5951.
19 D. Pierucci, H. Henck, J. Avila, A. Balan, C. H. Naylor, G. Patriarche, Y. J. Dappe, M. G. Silly, F. Sirotti, A. T. Johnson, M. C. Asensio and A. Ouerghi, *Nano Lett.*, 2016, **16**, 4054–4061.
20 R. I. Romanov, M. G. Kozodaev, Y. Y. Lebedinskii, I. V. Zabrosaev, E. A. Guberna and A. M. Markeev, *Phys. Status Solidi A*, 2021, **218**, 2000744.
21 H. Zeng, G. B. Liu, J. Dai, Y. Yan, B. Zhu, R. He, L. Xie, S. Xu, X. Chen, W. Yao and X. Cui, *Sci. Rep.*, 2013, **3**, 4908–4916.
22 D. Nam, J. U. Lee and H. Cheong, *Sci. Rep.*, 2015, **5**, 17113.

23 P. Soubelet, A. E. Bruchhausen, A. Fainstein, K. Nogajewski and C. Faugeras, *Phys. Rev. B*, 2016, **93**, 155407.

24 S. Tongay, J. Zhou, C. Ataca, K. Lo, T. S. Matthews, J. Li, J. C. Grossman and J. Wu, *Nano Lett.*, 2012, **12**, 5576–5580.

25 Y. Zhang, T. R. Chang, B. Zhou, Y. T. Cui, H. Yan, Z. Liu, F. Schmitt, J. Lee, R. Moore, Y. Chen, H. Lin, H. T. Jeng, S. K. Mo, Z. Hussain, A. Bansil and Z. X. Shen, *Nat. Nanotechnol.*, 2013, **9**, 111–115.

26 V. Babacic, D. S. Reig, S. Varghese, T. Vasileiadis, E. Coy, K.-J. Tielrooij and B. Graczykowski, *Adv. Mater.*, 2021, **33**, 2008614.

27 M. Cowie, R. Plougmann, Y. Benkirane, L. Schué, Z. Schumacher and P. Grütter, *Nanotechnology*, 2021, **33**, 125706.

28 X. Li, W. Cai, J. An, S. Kim, J. Nah, D. Yang, R. Piner, A. Velamakanni, I. Jung, E. Tutuc, S. K. Banerjee, L. Colombo and R. S. Ruoff, *Science*, 2009, **324**, 1312–1314.

29 J. Park, H. K. Park and J. Choi, *J. Phys. Chem. C*, 2017, **121**, 14954–14961.

30 H. K. Park and J. Choi, *ACS Photonics*, 2018, **5**, 2895–2903.

31 H. K. Park and J. Choi, *J. Mater. Chem. C*, 2018, **6**, 6958–6965.

32 Y. Meng, C. Ling, R. Xin, P. Wang, Y. Song, H. Bu, S. Gao, X. Wang, F. Song, J. Wang, X. Wang, B. Wang and G. Wang, *npj Quantum Mater.*, 2017, **2**, 16.

33 S. Barja, S. Refaely-Abramson, B. Schuler, D. Y. Qiu, A. Pulkin, S. Wickenburg, H. Ryu, M. M. Ugeda, C. Kastl, C. Chen, C. Hwang, A. Schwartzberg, S. Aloni, S. K. Mo, D. F. Ogletree, M. F. Crommie, O. V. Yazyev, S. G. Louie, J. B. Neaton and A. Weber-Bargioni, *Nat. Commun.*, 2019, **10**, 3382.

34 K. Momma and F. Izumi, *J. Appl. Cryst.*, 2011, **44**, 1272–1276.

35 J. Börner, P. Böttger, C. Kloc, D. R. T. Zahn, P. Tonndorf, O. Gordan, S. M. de Vasconcellos, A. Liebig, M. Albrecht, R. Bratschitsch, X. Zhang and R. Schmidt, *Opt. Express*, 2013, **21**, 4908–4916.

36 Y. Zhao, H. Lee, W. Choi, W. Fei and C. J. Lee, *RSC Adv.*, 2017, **7**, 27969–27973.

37 L. Pan, P. Miao, A. Horneber, A. J. Meixner, P. M. Adam and D. Zhang, *Beilstein J. Nanotechnol.*, 2022, **13**, 572–581.

38 J. Li, S. Wang, L. Li, Z. Wei, Q. Wang, H. Sun, J. Tian, Y. Guo, J. Liu, H. Yu, N. Li, G. Long, X. Bai, W. Yang, R. Yang, D. Shi and G. Zhang, *Small Sci.*, 2022, **2**, 2200062.

39 R. Fates, H. Bouridah and J. P. Raskin, *Carbon*, 2019, **149**, 390–399.

40 H. L. Liu, C. C. Shen, S. H. Su, C. L. Hsu, M. Y. Li and L. J. Li, *Appl. Phys. Lett.*, 2014, **105**, 201905.

41 H. L. Liu, T. Yang, J. H. Chen, H. W. Chen, H. Guo, R. Saito, M. Y. Li and L. J. Li, *Sci. Rep.*, 2020, **10**, 15282.

42 Y. Sata, R. Moriya, S. Morikawa, N. Yabuki, S. Masubuchi and T. Machida, *Appl. Phys. Lett.*, 2015, **107**, 023109.

43 S. K. Cheung and N. W. Cheung, *Appl. Phys. Lett.*, 1986, **49**, 85–87.

44 T. M. Mohiuddin, A. Lombardo, R. R. Nair, A. Bonetti, G. Savini, R. Jalil, N. Bonini, D. M. Basko, C. Galiotis, N. Marzari, K. S. Novoselov, A. K. Geim and A. C. Ferrari, *Phys. Rev. B: Condens. Matter Mater. Phys.*, 2009, **79**, 205433.

45 J. E. Lee, G. Ahn, J. Shim, Y. S. Lee and S. Ryu, *Nat. Commun.*, 2012, **3**, 1024.

46 A. C. Ferrari and D. M. Basko, *Nat. Nanotechnol.*, 2013, **8**, 235–246.

47 B. R. Borodin, F. A. Benimetskiy, M. S. Dunaevskiy, V. A. Sharov, A. N. Smirnov, V. Y. Davydov, E. L. hderanta, S. P. Lebedev, A. A. Lebedev and P. A. Alekseev, *Semicond. Sci. Technol.*, 2019, **34**, 125007.

48 D. N. Ortiz, I. Ramos, N. J. Pinto, M. Q. Zhao, V. Kumar and A. T. Johnson, *AIP Adv.*, 2018, **8**, 035014.

49 S. Refaely-Abramson, D. Y. Qiu, S. G. Louie and J. B. Neaton, *Phys. Rev. Lett.*, 2018, **121**, 167402.